One-Step Low Temperature Hydrothermal Synthesis of Flexible TiO$_2$/PVDF@MoS$_2$ Core-Shell Heterostructured Fibers for Visible-Light-Driven Photocatalysis and Self-Cleaning

Zhi-Guang Zhang [1,2]**, Hui Liu** [1]**, Xiao-Xiong Wang** [1]**, Jun Zhang** [1]**, Miao Yu** [1,3]**,
Seeram Ramakrishna** [4] **and Yun-Ze Long** [1,*]

[1] Collaborative Innovation Center for Nanomaterials & Devices, College of Physics, Qingdao University, Qingdao 266071, China; zhangzhiguangphysics@126.com (Z.-G.Z.); lhqddx@163.com (H.L.); wangxiaoxiong69@163.com (X.-X.W.); iamjunzhang@163.com (J.Z.); my2373@columbia.edu (M.Y.)

[2] College of Science & Information, Qingdao Agricultural University, Qingdao 266109, China

[3] Department of Mechanical Engineering, Columbia University, New York, NY 10027, USA

[4] Center for Nanofibers & Nanotechnology, Nanoscience & Nanotechnology Initiative, Faculty of Engineering, National University of Singapore, Singapore 117576, Singapore; seeram@nus.edu.sg

[*] Correspondence: yunze.long@163.com or yunze.long@qdu.edu.cn; Tel.: +86-139-5329-0681; Fax: +86-532-8595-5977

check for updates

Abstract: Novel flexible and recyclable core-shell heterostructured fibers based on cauliflower-like MoS$_2$ and TiO$_2$/PVDF fibers have been designed through one-step hydrothermal treatment based on electrospun tetrabutyl orthotitanate (TBOT)/PVDF fibers. The low hydrothermal temperature avoids the high temperature process and keeps the flexibility of the as-synthesized materials. The formation mechanism of the resultant product is discussed in detail. The composite of MoS$_2$ not only expands the light harvesting window to include visible light, but also increases the separation efficiency of photo-generated electrons and holes. The as-prepared product has proven to possess excellent and stable photocatalytic activity in the degradation of Rhodamine B and levofloxacin hydrochloride under visible light irradiation. In addition, the TiO$_2$/PVDF@MoS$_2$ core-shell heterostructured fibers exhibit self-cleaning property to dye droplets under visible light irradiation. Meanwhile, due to its hydrophobicity, the resultant product can automatically remove dust on its surface under the rolling condition of droplets. Hence, the as-prepared product cannot only degrade the contaminated compounds on the surface of the material, but also reduce the maintenance cost of the material due to its self-cleaning performance. Therefore, the as-prepared product possesses potential applications in degradation of organic pollutants and water treatment, which makes it a prospective material in the field of environmental treatment.

Keywords: low temperature; core-shell heterostructure; visible light; photocatalysis; self-cleaning

1. Introduction

As a highly efficient, economical and environmentally friendly "green" technology, photocatalysis offers tremendous potential for environmental protection and energy conversion. Therefore, the production of advanced photocatalytic materials is one of the main strategies to solve the current global environmental needs [1,2]. Titanium dioxide (TiO$_2$) has proven to be a promising candidate for photocatalysts in various transition metal oxide semiconductors over the past few decades due to its good physicochemical properties, non-toxicity, low-cost, stable chemical and

photonic properties [3]. However, as an n-type wide-bandgap semiconductor, TiO_2 absorbs only ultraviolet light, which accounts for only 4% of total sunlight in the solar spectrum. In addition, the recombination rate of photo-generated electron hole pairs in TiO_2 is high, resulting in low quantum efficiency and low photocatalytic activity. Furthermore, for the traditional powder-like photocatalyst, it is also very difficult to separate and recover a photocatalyst from the reaction solution after the photocatalytic reaction.

Therefore, the key for preparation of a highly active and recyclable TiO_2-based photocatalyst is to find a strategy for inhibiting photo-generated electron-hole recombination, narrowing the band gap and easy recovery and recycle. To this end, many strategies have been developed, one of which is the composition of narrow band gap semiconductors to TiO_2 to form a heterogeneous structure [4–6]. On the one hand, the composition of narrow band gap semiconductors can improve the photocatalytic activity of TiO_2-based photocatalysts by expanding their light capture window to the visible range [7]. On the other hand, the heterostructure between narrow band gap semiconductors and TiO_2 can also enhance the charge separation by coupling two semiconductor structures with matched energy levels, thereby increasing the photocatalytic activity and efficiency of the TiO_2-based photocatalyst [8,9]. Among many narrow bandgap semiconductors, molybdenum disulfide (MoS_2) has become the material of choice for composite heterostructures due to its large reserves, low cost, and excellent electronic and optical properties [10–12]. Zheng et al. synthesized hierarchical MoS_2 nanosheet@TiO_2 nanotube arrays by combining the anodic oxidation method and hydrothermal method [13]. The as-prepared hierarchical composite materials are of enhanced photocatalytic and photocurrent performances. Liu et al. prepared 3D sandwich-like heterojunction structured mesoporous black TiO_2/MoS_2/TiO_2 nanosheets which have 89.86% methyl orange degradation rate and 0.56 mmol·h^{-1}·g^{-1} hydrogen production rate [14]. However, the above-mentioned several kinds of composite photocatalysts still exist in the form of powder. Therefore, there is still a disadvantage for recovery and recycle when the photocatalyst was used in a reaction solution. In order to improve the recovery and recycle of a photocatalyst, the method of supporting the photocatalytic material on an inorganic porous material or a polymer material has been reported [15–18]. Zhang et al. fabricated 3D MoS_2 nanosheet/TiO_2 nanofiber heterostructures by using the electrospinning method combined with hydrothermal treatment [19]. The as-synthesized fibers presented enhanced performance in the photocatalytic decomposition of organic dyes under UV light irradiation. However, a high temperature post-sintering process was employed in the synthesis procedure to remove the polymer composition, which resulted in the as-synthesized nanofibers being too fragile and difficult to reuse [20]. In order to solve the problem of difficult to recover photocatalysts, flexible substrate materials have been introduced as photocatalyst carriers [21–24]. Lin et al. synthesized a novel floating sheet used in solar photocatalytic water splitting. The as-synthesized novel floating sheet consists of WSe_2 film laser-deposited on a carbon foam substrate and nanodiamond-embedded Cu_2O photocatalysts, which has better reusability [21]. Yu et al. synthesized AgX (X = Br, I)-TiO_2 nanoparticles immobilized on polyacrilonitrile (PAN) nanofibers by combining the electrospinning technique, solvothermal synthesis, physical adsorption, and gas/solid reaction. The as-prepared composite showed excellent visible light catalytic performance against various pollutants [24]. Polyvinylidene difluoride (PVDF), a widely used commercial polymer material, which has the advantages of good thermal stability, high mechanical strength, and chemical resistance, is very suitable as a carrier for flexible composite materials [25]. Our previous work showed that the use of PVDF as photocatalyst carrier can be a good solution for the separation and recovery of photocatalysts from the reaction solution [26].

In this paper, novel flexible, recyclable, and reusable TiO_2/PVDF@MoS_2 core-shell heterostructured fibers were synthesized by one-step hydrothermal treatment at low temperature based on electrospun tetrabutyl orthotitanate (TBOT)/PVDF fibers. The one-step hydrothermal method is very simple and feasible. In addition, the low hydrothermal temperature, avoiding the high temperature process, will not damage the flexibility of the as-synthesized materials. A large number of cauliflower-like MoS_2 nanoparticles were grown on the surface of TiO_2/PVDF fibers forming

a flexible core-shell heterostructure. The as-prepared materials have good flexibility, recyclability, and reusable property. The mechanism that the flexible TiO_2/PVDF@MoS_2 core-shell heterostructured fibers have excellent photocatalytic activity on organic pollutants under visible light was discussed. The self-cleaning properties of the resultant product were also investigated. The results show that the photocatalytic activity of TiO_2 crystal is significantly increased in the presence of MoS_2 as a co-catalyst. Furthermore, the as-prepared product cannot only degrade the contaminated compounds on the surface of the material, but also reduce the maintenance cost of the material due to its self-cleaning performance. Therefore, the application of flexible TiO_2/PVDF@MoS_2 core-shell heterostructured fibers to the decomposition of toxic and harmful organic pollutants is of great significance for environmental protection.

2. Experimental

2.1. Materials

PVDF (FR904) was purchased from Shanghai 3F New Materials Co., Ltd. (Shanghai, China), Degussa P25 (80% anatase and 20% rutile) was purchased from Evonik Degussa Company (Shanghai, China), *N*,*N*-dimethylformamide (DMF, AR, 99.5%), acetone (CP, 99.0%), sulphuric acid (H_2SO_4, CP, 95.0%~98.0%), TBOT(CP, 98.0%), Sodium molybdate dihydrate ($Na_2MoO_4 \cdot 2H_2O$, AR, 99.0%) and thiourea (AR, 99.0%) were purchased from Sinopharm Chemical Reagent Co., Ltd. (Shanghai, China). All reagents were used as received without any further purification.

2.2. Preparation of TBOT/PVDF Fibers

A 4.0 g sample of PVDF powder was added into a mixture of solvents with 10 g DMF and 10 g acetone and stirred vigorously at 40 °C until the solution was clear and transparent. Then, 10 mL of TBOT was added to the clear solution and stirring was continued for 1 h at 40 °C. Electrospinning was operated using a 5 mL syringe containing the TBOT/PVDF precursor solution with a blunt metal needle. The fiber collector was a stainless steel roller wrapped with a sheet of aluminum foil and operating a rotation speed of about 250 rpm. A DC voltage supply with a setting of 9 kV was placed between the needle tip and the collector with the needle tip and collector at a distance of 11 cm. The fibrous mats collected on the aluminium foils were dried at 60 °C for 10 h after spinning to eliminate any remaining solvent. All the as-prepared TBOT/PVDF fibers were cut into small pieces of 2.5 cm × 2.5 cm for the hydrothermal treatment.

2.3. Fabrication of TiO_2/PVDF@MoS_2 Core-Shell Heterostructured Fibers

0.5 mmol $Na_2MoO_4 \cdot 2H_2O$ and 2.5 mmol thiourea were added into 30 mL of 0.5 M sulfuric acid solution and stirred for 30 min. The solution was then transferred to a 50 mL stainless steel autoclave. The TBOT/PVDF small pieces were then placed into the stainless steel autoclave. The hydrothermal reaction was carried out at 150 °C for 24 h, and then the flexible TiO_2/PVDF@MoS_2 core-shell heterostructured fibers were obtained. For comparison, the same conditions were carried out without Mo source and S source to form TiO_2/PVDF fibrous mat, and the same conditions using PVDF fibers mat to form MoS_2/PVDF fibrous mat. The as-obtained fibers mats were thoroughly washed with ethyl alcohol and deionized water, followed by drying in air at 60 °C for 10 h after the hydrothermal treatment.

2.4. Characterization

X-ray diffraction (XRD) patterns were taken with a Rigaku SmartLab X-ray diffractometer (Rigaku, Tokyo, Japan) using a Cu-Kα radiation in the 2θ range of 10–80° at room temperature. The scanning electron microscopy (SEM) images of the as-synthesized samples were taken using a JEOL JSM-7800F field emission scanning electron microscope (JEOL, Tokyo, Japan). A JEOL JEM-2100Plus transmission electron microscopy (TEM) (JEOL, Tokyo, Japan) attached energy dispersive spectroscopy

(EDS) was used for observation of the as-obtained samples. X-ray photoelectron spectroscopy (XPS) measurements were carried out on a Thermo Scientific Escalab 250Xi system (Thermo Scientific, Shanghai, China) with an Al Kα X-ray source. The Brunauer-Emmett-Teller (BET) specific surface area was performed on a Quantachrome Autosorb-IQ-MP/XR nitrogen adsorption apparatus (Quantachrome, Shanghai, China). UV-Vis diffuse reflectance spectra (DRS) of the as-prepared samples were taken using a Shimadzu UV-2600 spectrophotometer (Shimadzu, Tokyo, Japan) with an integrating sphere accessory, in which $BaSO_4$ was utilized as a diffuse reflectance standard. A Hitachi F-2500 fluorescence spectrometer (Hitachi, Tokyo, Japan) with a Xe lamp was used to determine the photoluminescence spectra (PL) of the resultant membranes using 320 nm as the excitation wavelength at room temperature.

2.5. Photocatalytic Activity

The photocatalytic performances of the as-synthesized samples were evaluated by decomposing the model pollutants rhodamineB (RhB, 15 mg·L^{-1}) and levofloxacin hydrochloride (LVFX, 5 mg·L^{-1}) under visible-light irradiation at room temperature. In order to compare the photocatalytic ability to degrade dye contaminants, Degussa P25 was purchased and applied to the degradation of RhB photocatalytic experiments. In photodegradation experiments, the photocatalysts (1 g·L^{-1}) were put into a 100 mL quartz tube with 60 mL target pollutants solution and magnetically stirred in the dark for 45 min to ensure the adsorption-desorption equilibrium of target pollutants on the catalysts surface. Then this system was placed under a 9 W white light LED (Figure S1, Supporting Information (SI)) with a distance of 4.0 cm apart away from the quartz tube where the power density of the white LED lamp is 0.9 mW·cm^{-2}. At selected time intervals, 3 mL of aliquots were collected and centrifuged to remove the particles, then sampled to analyze the concentration of RhB remaining in the solution by measuring its absorbance at 554 nm for RhB (292 nm for LVFX) using a Shimadzu UV-2600 spectrophotometer. For the membranes reaction system, the analyzed aliquot was quickly poured back into the quartz tube to ensure a roughly equivalent volume of solution after every assay. The photodegradation efficiency was expressed as C/C_0, where C is the absorption of RhB absorption spectrum at 554 nm (292 nm for LVFX) at selected time intervals and C_0 is the absorption of the starting concentration. In order to investigate the recycle stability, the as-prepared TiO_2/PVDF@MoS_2 core-shell heterostructured fibers were washed with ethyl alcohol and deionized water, and then dried in air for the next photodegradation process.

Control experiments on the photodegradation of RhB were carried out by using ethylene diamine tetraacetic acid (EDTA, 10 mM), tertiary butanol (tBuOH, 10 mM) and nitrogen (N_2) as the photo-generated holes (h$^+$), the hydroxyl radicals (OH$^\bullet$) and the superoxide anion radicals ($O_2^{-\bullet}$) scavenger, respectively.

2.6. Self-Cleaning Performance

2.6.1. Hydrophobicity Property

The hydrophobicity of the TiO_2/PVDF@MoS_2 core-shell heterostructured fibers is evaluated by measuring the contact angle of the droplets (including H_2O, RhB, methylene blue (MB)) on the material under ambient temperature. The water contact angle measurements were carried out by the drop method on a Theta Attension optical contact angle instrument (Biolin Scientific, Stockholm, Sweden).

2.6.2. Fading of Dye Droplets

The RhB and MB dye droplets with a concentration of 10 mg·L^{-1} were dripped onto the TiO_2/PVDF@MoS_2 core-shell heterostructured fibers and irradiated under visible light. An optical photograph was taken every 25 min to compare the color of the dye, which was used to characterize the self-cleaning performance of the as-prepared product to the surface colored pollutants.

2.6.3. Removal of Dust on Sample Surface

In order to evaluate the self-cleaning effect of the TiO_2/PVDF@MoS_2 core-shell heterostructured fibers on the dust on its surface, the dust was scattered on the surface of the sample before measurement. Then, a drop of water was dropped on the surface of the sample. Tilted the sample slightly to make the droplet move on the sample surface and take away the dust, thus making the material surface clean.

3. Results and Discussion

3.1. Synthesis and Application Process

A brief synthesis and application process of TiO_2/PVDF@MoS_2 core-shell heterostructured fibers are depicted in Figure 1. Firstly, the TBOT/PVDF fibrous mat was obtained by electrospinning TBOT/PVDF homogeneous solution. Secondly, the as-prepared TBOT/PVDF fibrous mat was cut into small pieces, followed by hydrothermal treatment to synthesize flexible TiO_2/PVDF@MoS_2 core-shell heterostructured fibers. Thirdly, the flexible TiO_2/PVDF@MoS_2 core-shell heterostructured fibers were applied to degrade organic pollutant under visible light. Finally, the flexible TiO_2/PVDF@MoS_2 core-shell heterostructured fibers were drawn out from the reaction system and thoroughly washed with ethyl alcohol and deionized water, followed by drying in air at 60 °C for 10 h for the next photocatalytic experiment.
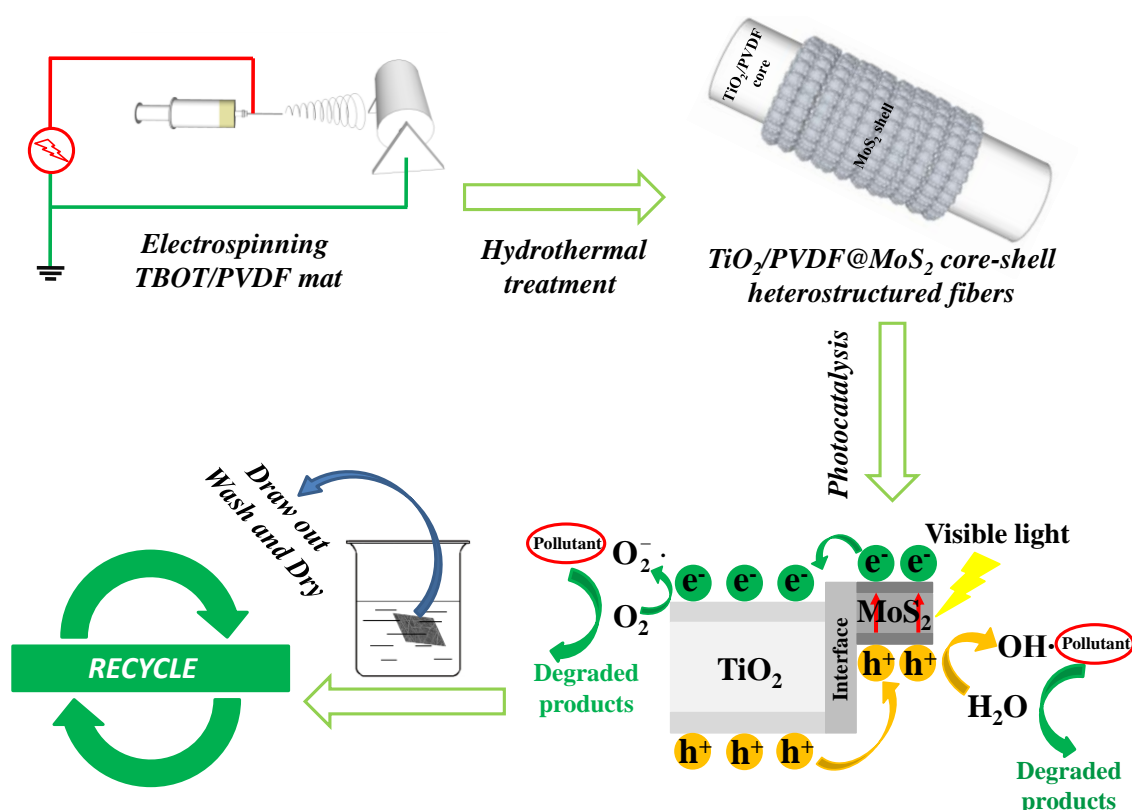

Figure 1. Schematic illustration for the synthesis and application process of TiO_2/PVDF@MoS_2 core-shell heterostructured fibers.

3.2. Structure and Morphology Characteristics

Figure 2 depicts the X-ray diffraction (XRD) patterns of the as-prepared samples. As displayed in Figure 2 curve (a), no obvious diffraction peak was detected except the diffraction peak 2θ at 20.7° which can be assigned to the β phase of PVDF [27,28]. This means that the TiO_2 small crystal in the TBOT/PVDF hybrid fibers mat, formed through TBOT hydrolyzed with the H_2O in air,

was mainly in the amorphous structure. After hydrothermal reaction in 0.5 M H_2SO_4 at 150 °C for 24 h, the characteristic diffraction peaks of anatase phase TiO_2 (PDF card 89-4921, Joint Committee on Powder Diffraction Standards (JCPDS)) appeared in the prepared hybrid material, whose diffraction peaks 2θ at 25.6, 37.9, 48.2, 54.4, and 62.8° as shown in the curve (b). The addition of H_2SO_4 ensured the formation of anatase phase TiO_2 [29]. In addition to the above-mentioned anatase phase TiO_2 diffraction peaks in the curve (b), a weak and broad diffraction peak at 14.4° can be detected in the curve (c), which can be indexed to the (002) crystal face of MoS_2 (PDF card 37-1492, JCPDS). Comparing curve (c) with curve (a) and (b), it can be seen that the intensity of the diffraction peaks of PVDF and anatase TiO_2 decreased after synthesizing MoS_2 on TiO_2/PVDF fibers, indicating that the surface area of TiO_2/PVDF was covered with MoS_2 that forms a core-shell structure. In order to further determine whether the preparation of MoS_2 was successful, the powder in the hydrothermal autoclave was centrifuged after hydrothermal reaction and tested (shown in curve (d)). Comparing curves (d) with (c), it was obvious that all the diffraction peaks were at the same position except the diffraction peaks of PVDF especially, where the diffraction peak of MoS_2 became stronger, indicating the MoS_2 was synthesized successfully. As a comparison, the XRD patterns of pure PVDF fibers mat, MoS_2/PVDF hybrid fibers mat and MoS_2 powder remaining in the hydrothermal autoclave after hydrothermal synthesizing MoS_2/PVDF hybrid fibers mat were displayed in Figure S2 (SI). It can be concluded the MoS_2 was successfully grown on the PVDF fibers.
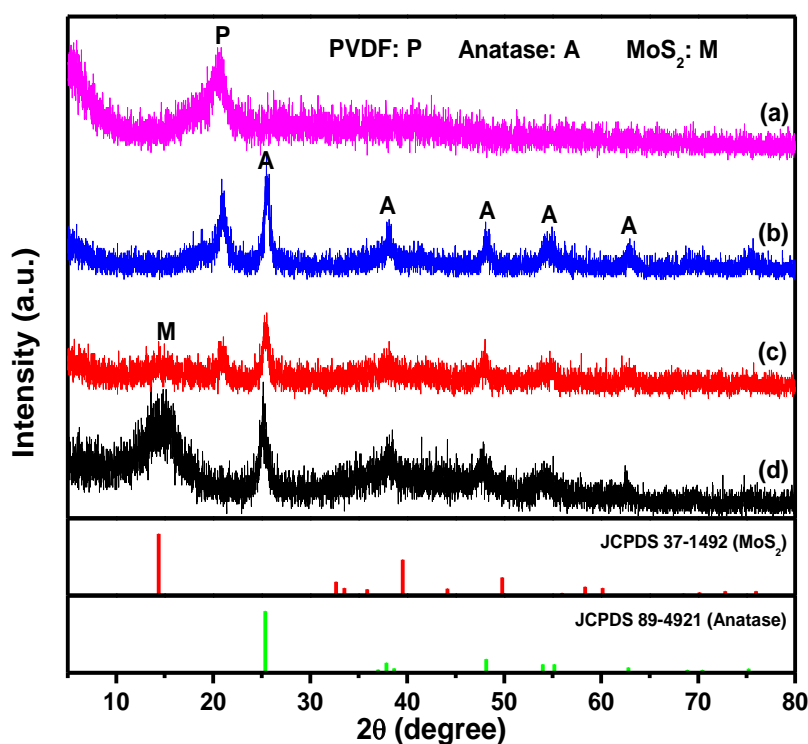

Figure 2. XRD patterns of (**a**) TBOT/PVDF fibers, (**b**) TiO_2/PVDF hybrid fibers, (**c**) TiO_2/PVDF@MoS_2 core-shell heterostructured fibers, and (**d**) MoS_2 and TiO_2 powders.

Figure 3 shows the typical SEM images of TBOT/PVDF fibers, TiO_2/PVDF fibers and TiO_2/PVDF@MoS_2 core-shell heterostructured fibers, respectively. As illustrated in Figure 3a, TBOT/PVDF fibers randomly distributed with a rough surface different from pure PVDF fibers synthesized in our previous work [26], mainly due to the TBOT component in the fibers hydrolyzed with the H_2O in the atmosphere. It can be seen from Figure 3a that the fiber diameter distribution was very uneven, some particularly thick and some particularly fine. Besides, it is obvious that some fibers were broken, and the same phenomenon also appeared in Figure 3b,c. Considering the blend of

PVDF polymer and TBOT in the precursor solution, the spinning needle would be blocked, caused by the hydrolysis reaction between TBOT and H_2O in the air during the electrospinning process, which would lead to the diameter distribution of fibers nonuniform. While the TBOT component in the fibers continuing to hydrolyze with H_2O in the air will cause fiber fracture. After being hydrolyzed in 0.5 M H_2SO_4 at 150 °C for 24 h, anatase phase TiO_2 occurred on the fiber surface (shown in Figure 3b), which can be confirmed by the XRD patterns. As depicted in Figure 3b, anatase phase TiO_2 particles with irregular shapes and sizes were randomly distributed on the fibers surface. During hydrothermal growth process, a portion of the TBOT component in the fibers dissolved in the reaction liquid while the other part remained in the fibers. In an acid solution environment, both of them began to hydrolyze to form TiO_2 at the same time. Due to the lack of nucleation centers in the liquid, a part of the TBOT dissolved in the liquid hydrolyzed and grew homogeneously to form TiO_2 powder directly, and the other part combined with the TiO_2 particles formed by TBOT hydrolysis in the fiber to become larger particles. As a result, morphology as shown in Figure 3b was formed.
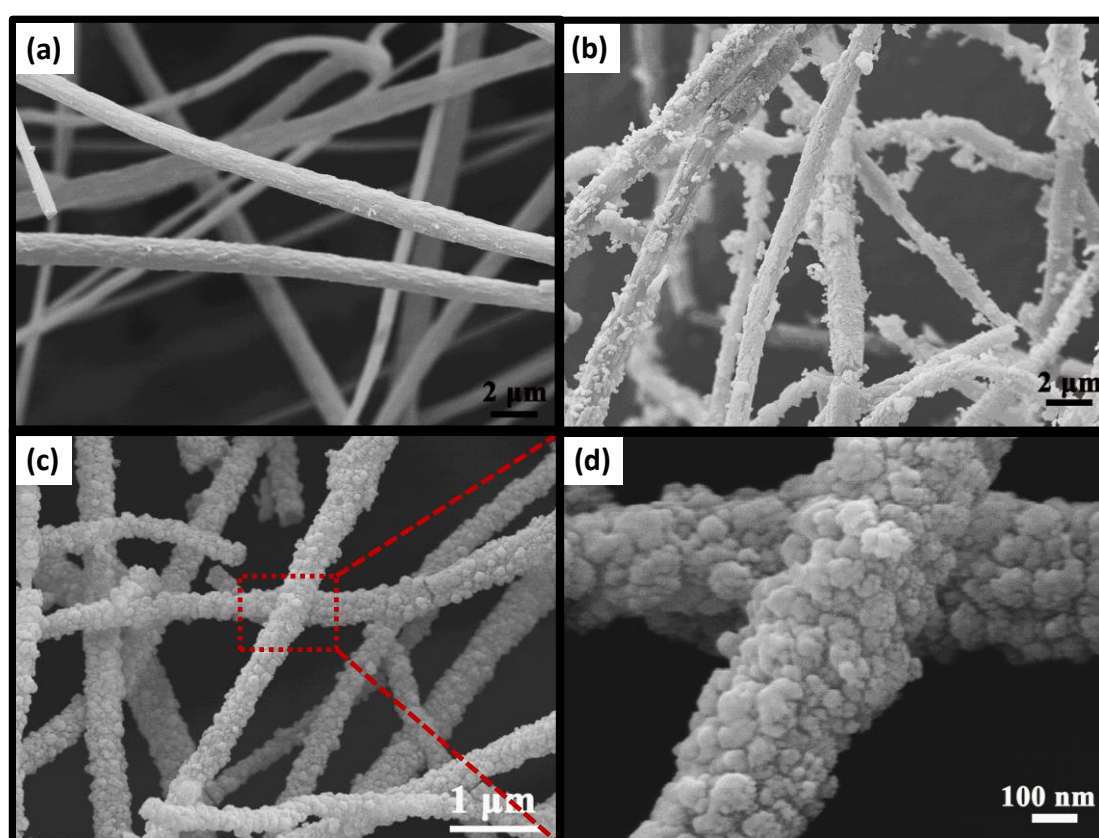

Figure 3. SEM images of (**a**) TBOT/PVDF fibers, (**b**) TiO_2/PVDF fibers, (**c**) TiO_2/PVDF@MoS_2 fibers, and (**d**) high resolution SEM image of TiO_2/PVDF@MoS_2 core-shell heterostructured fibers.

As presented in Figure 3c,d, unlike the common layered structure of MoS_2, a large number of cauliflower MoS_2 particles appeared on the fibers surface forming core-shell structure. In contrast to the morphology of the TiO_2 particles in Figure 3b, these cauliflower MoS_2 particles were relatively uniform and dense. For TiO_2/PVDF@MoS_2 fibers, the hydrolysis of TBOT and the growth of MoS_2 were carried out simultaneously. Since there were many MoS_2 particles in the solution, this makes the TiO_2 in the liquid hydrolyzed by TBOT more likely to combine with the MoS_2 to form heterogeneous growth rather than to grow on the fibers. Therefore, no particularly large TiO_2 particles were formed on the fibers. The amount of Na_2MoO_4 and $(H_2N)_2CS$ in the solution was sufficient so that MoS_2 can either directly form a powder in solution or grow on the surface of the TiO_2/PVDF core, which was the main reason for the difference in topography between Figure 3b,c.

The morphology of TiO_2/PVDF@MoS_2 core-shell heterostructured fiber was further confirmed by TEM and HRTEM, as shown in Figure 4. It is clearly observed that the very fine MoS_2 particle grew on the surface of TiO_2/PVDF fiber and core–shell structures appeared, as displayed in Figure 4a. The high-resolution TEM image showed that the MoS_2 particles with several layer thicknesses were about 5 nm in size. In addition, the MoS_2 particles with an average spacing of 0.61 nm can be seen, which belongs to the (002) facet of MoS_2 [30–32]. In Figure 4b, the lattice spacing of TiO_2 was measured to be 0.35 nm, which was in close agreement with (101) facets of anatase TiO_2 [33]. The lattice spacing shown in the HRTEM images is consistent with the XRD results, further confirming the formation of TiO_2/PVDF@MoS_2 core-shell structure.
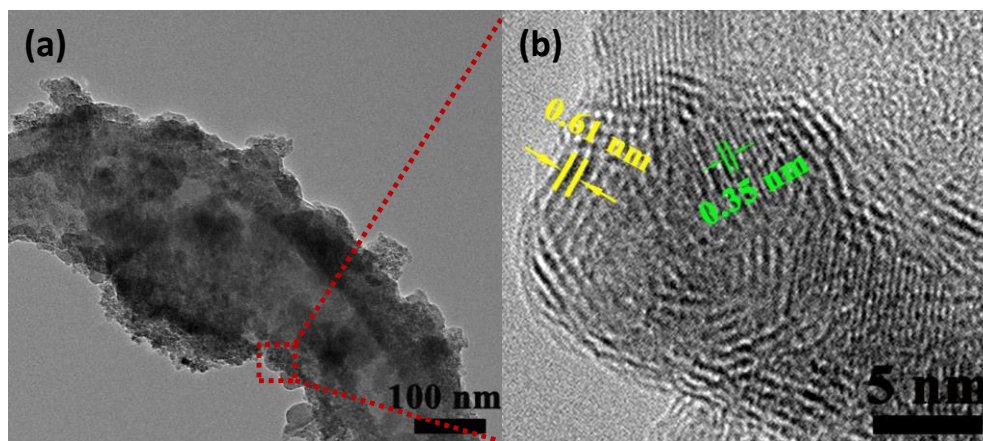
Figure 4. TEM image of TiO_2/PVDF@MoS_2 core-shell heterostructured fiber (**a**) and high-resolution TEM image of TiO_2/PVDF@MoS_2 core-shell heterostructured fiber (**b**).

The EDS technique was employed for further detecting the elemental composition of as-prepared TiO_2/PVDF@MoS_2 fiber. The EDS spectroscopy in Figure S3 (SI) displays the elements of C, O, F, Cu, Ti, S, and Mo, of which Cu was from copper mesh brackets, confirming the presence of PVDF, TiO_2, and MoS_2.

The chemical composition information and the bonding configuration of the as-prepared products were determined by XPS analysis. Characteristic peaks from Mo, S, O, Ti, F, and C can be clearly found from the XPS survey spectra, as shown in Figure S4 (SI). Figure 5 illustrates the high-resolution XPS spectra of Ti 2p, O 1s, Mo 3d, and S 2p. As shown in Figure 5a, the binding energies of Ti $2p_{3/2}$ and Ti $2p_{1/2}$ peaks were located at 459.0 and 464.6 eV, respectively [34]. The peak of O1s was broken up into four peaks (shown in Figure 5b), respectively, corresponding to Ti-O of TiO_2 (530.2 eV), Ti-O-Mo bonds between MoS_2 and TiO_2 (530.8 eV), hydroxyl group (531.7 eV), and C-O bond (532.6 eV) in the resultant product [35–37]. In Mo 3d profiles (Figure 5c), the peaks at 232.6 and 229.3 eV were corresponding to $3d_{3/2}$ and $3d_{5/2}$ of Mo^{4+}, respectively. And the satellite-peak at 227.2 eV ascribed to 2s of S species [38]. Meanwhile, the peaks of S element could be divided into three different chemical environments, as displayed in Figure 5d. The broad spectra could be fitted with sets of doublets related to spin orbit split to $2p_{3/2}$ and $2p_{1/2}$. The peaks at binding energies of 162.4 and 163.7 eV were assigned to the $2p_{3/2}$ and $2p_{1/2}$ of S^{2-} [13]. Whereas, the peaks at 163.3 and 164.4 eV may be assigned to C-S bonds or related to the presence of bridging S_2^{2-} [39,40]. Besides, the weak peak at 168.9 eV was related to the residual of SO_4^{2-} in the as-prepared sample [41,42]. These results further confirmed the presence of MoS_2, TiO_2, and PVDF, which agreed well with the XRD and TEM results.
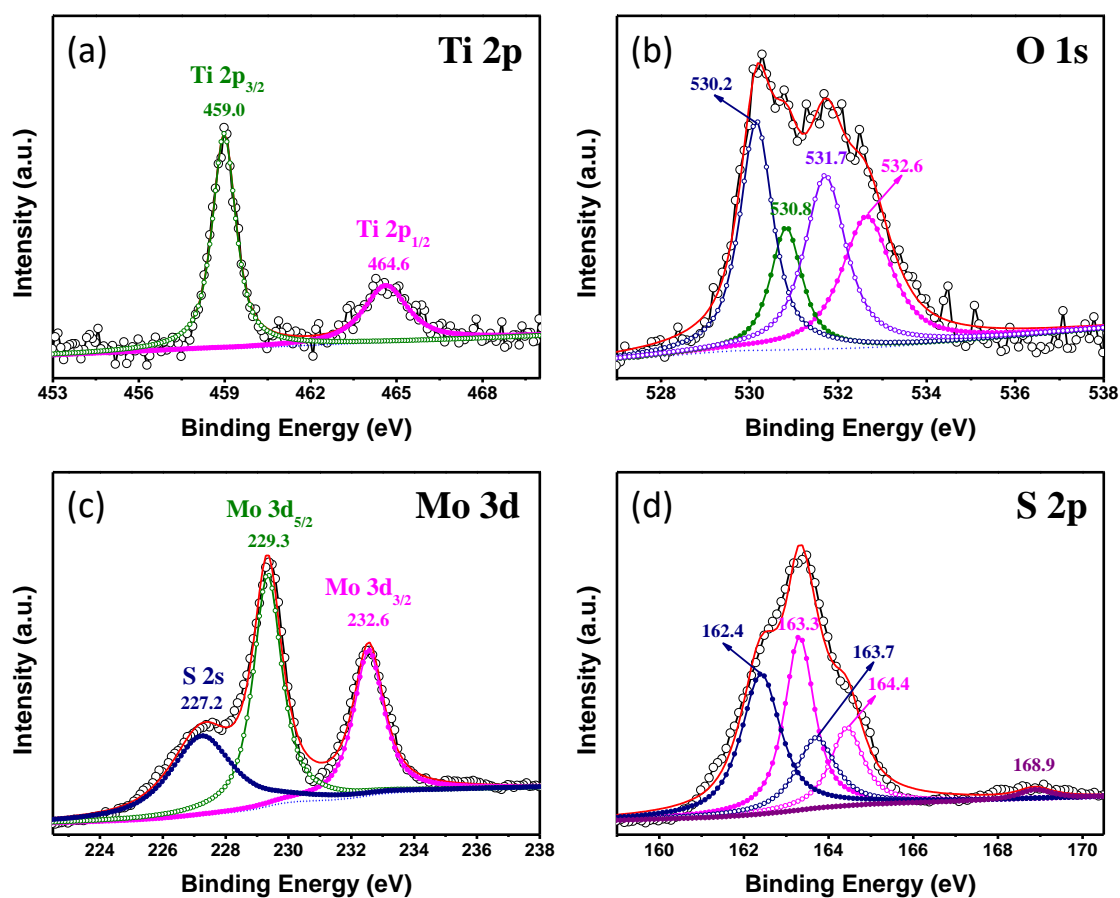
Figure 5. High-resolution XPS spectra of (**a**) Ti 2p, (**b**) O 1s, (**c**) Mo 3d and (**d**) S 2p in $TiO_2/PVDF@MoS_2$ core-shell heterostructured fiber.

To investigate the specific surface area of resultant products, nitrogen adsorption-desorption analysis was carried out by using the BET method. Figure 6 displays the nitrogen adsorption–desorption isotherms of $TiO_2/PVDF$ and $TiO_2/PVDF@MoS_2$ fibers, and the inset illustrates the corresponding pore diameter distribution by using the Barrett-Joyner-Halenda (BJH) method. The isotherm curves of $TiO_2/PVDF$ and $TiO_2/PVDF@MoS_2$ fibers were well in agreement with the type IV isotherm behavior with H3 hysteresis [43,44].

The surface area of $TiO_2/PVDF$ fibers was 49.5 $m^2 \cdot g^{-1}$, whereas the $TiO_2/PVDF@MoS_2$ core-shell heterostructured fibers had a surface area of 59.2 $m^2 \cdot g^{-1}$. Meanwhile, the pore diameter distribution of $TiO_2/PVDF$ and $TiO_2/PVDF@MoS_2$ core-shell heterostructured fibers was very irregular, as shown in the inset of Figure 6. Compared to the $TiO_2/PVDF$ fibers, the pore diameter distribution of $TiO_2/PVDF@MoS_2$ core-shell heterostructured fibers tended to be smaller, mainly due to the fact that the surface of $TiO_2/PVDF$ fibers was covered with smaller MoS_2 particles instead of larger TiO_2 particles, which was consistent with the SEM results. Hence, the as-obtained $TiO_2/PVDF@MoS_2$ core-shell heterostructured fibers possessed much more absorption interface.
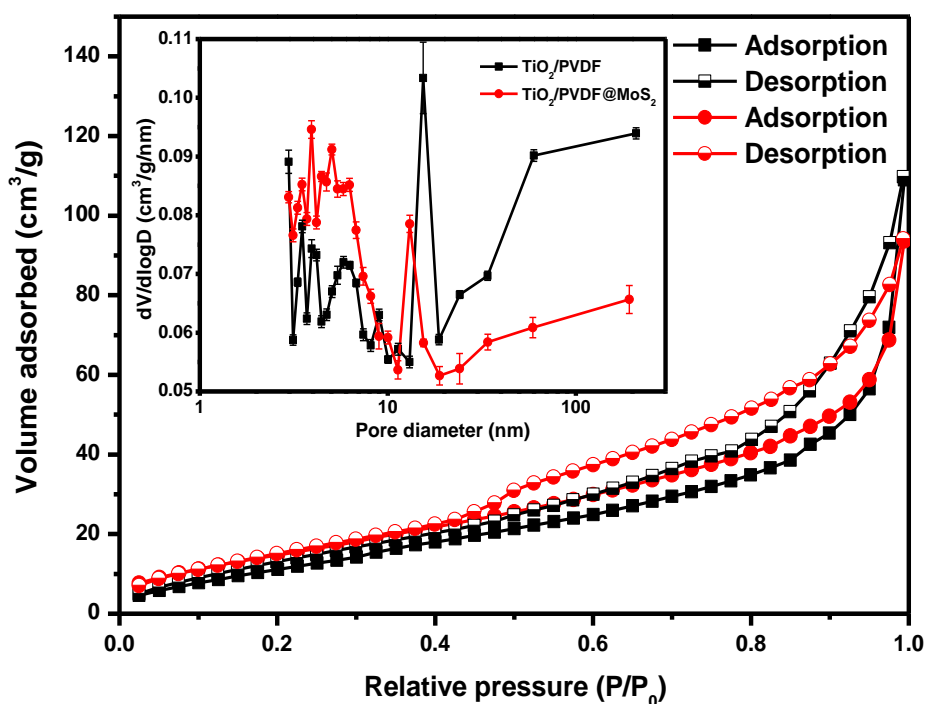
Figure 6. Nitrogen adsorption–desorption isotherms and the corresponding pore-diameter distribution curves (inset) of TiO_2/PVDF (Black line) and TiO_2/PVDF@MoS_2 core-shell heterostructured fibers (Red line).

3.3. Optical Characteristics

Optical absorption of P25, PVDF, MoS_2/PVDF, TBOT/PVDF, TiO_2/PVDF, and TiO_2/PVDF@MoS_2 were investigated by UV-Vis diffuse reflectance spectra, displayed in Figure 7. It can be found that all materials had a strong absorption except PVDF at wavelengths below 400 nm. Most especially, the TBOT/PVDF fibers had the strongest absorption in the ultraviolet region, owing to formation of amorphous structured TiO_2 crystal through TBOT hydrolyzed with the H_2O in air. In the visible light region, the samples with MoS_2 particles covered on the surface present enhanced absorption character compared to P25 and TiO_2/PVDF fibers.

For an indirect-band-gap semiconductor, the band-gap energy can be acquired by equation $Eg = 1240/\lambda_g$ (eV), where λ_g is the absorption edge calculated from the intercept between the tangent of the absorption curve and the abscissa coordinate [45]. The absorption edge and band-gap energy for P25, TBOT/PVDF, TiO_2/PVDF, MoS_2/PVDF, and TiO_2/PVDF@ MoS_2 was displayed in Table 1. Obviously, the band-gap energy of the TiO_2/PVDF@ MoS_2 was different from the MoS_2/PVDF and the TiO_2/PVDF, mainly due to its core-shell structure [46].
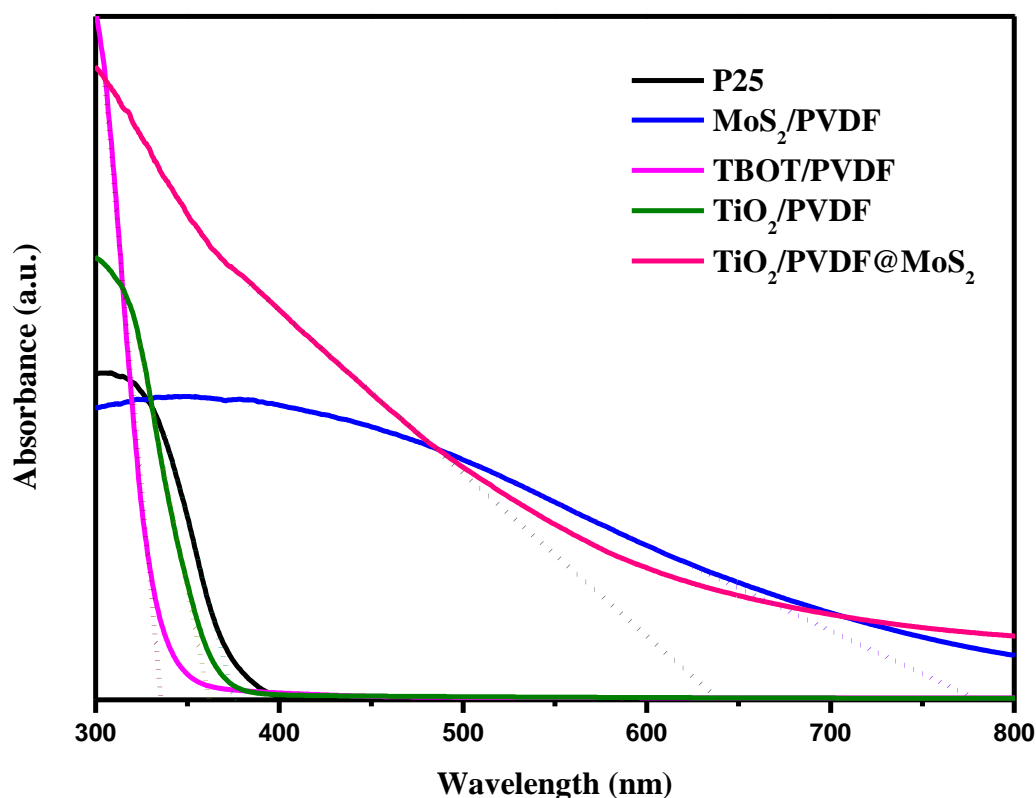
Figure 7. UV-vis diffuses reflectance spectra of different samples: P25, PVDF, MoS$_2$/PVDF, TBOT/PVDF, TiO$_2$/PVDF and TiO$_2$/PVDF@MoS$_2$.

Table 1. The absorption edge and energy band gap for the typical samples.

Typical Sample	Absorption Edge (nm)	Energy Band Gap (eV)
MoS$_2$/PVDF	780.4	1.6
TiO$_2$/PVDF@ MoS$_2$	639.3	1.9
P25	375.7	3.3
TiO$_2$/PVDF	361.8	3.4
TBOT/PVDF	335.5	3.7

Benefitting from the addition of narrow band gap MoS$_2$, the absorption edge of TiO$_2$/PVDF@ MoS$_2$ core-shell heterostructured fibers shifted to longer wavelength (1.9 eV) compared to that of TiO$_2$/PVDF fibers at 3.4 eV. Therefore, the core-shell heterostructured TiO$_2$/PVDF@ MoS$_2$ fibers offered enhanced light harvesting in the visible region of the solar spectrum, and thus, presented considerable photocatalytic abilities under visible light illumination.

The photoluminescence (PL) spectra were usually used to evaluate the efficiency of charge trapping and recombination of photo-induced electron-hole pairs in the semiconductor [47,48]. Figure 8 shows the PL spectra of P25, TiO$_2$/PVDF, MoS$_2$/PVDF, and TiO$_2$/PVDF@MoS$_2$. There were four main emission peaks for P25 and TiO$_2$/PVDF, respectively. The peak located at 398 nm ($\approx$3.12 eV) belonged to P25; meanwhile, the peaks located at 386 nm ($\approx$3.21 eV) belonged to TiO$_2$/PVDF. The other three peaks, located at 448 nm ($\approx$2.77 eV), 465 nm (2.67 eV) and 487 nm ($\approx$2.55 eV), respectively, appear in both P25 and TiO$_2$/PVDF. The first peak of these two materials corresponded to their near-band gap emission [26], whereas the other three peaks were likely assigned to the emission of oxygen vacancies related defect formed in the synthetic process [49–51]. Besides, it is obviously that P25 has the highest PL intensity, which means having the highest photo-generated electron-hole recombination. Interestingly, the PL intensity of TiO$_2$/PVDF fibers was weaker than that of P25, implying a relatively higher photo-generated electron-hole separation efficiency. The formation of F-Ti

coordination bond in the fibers and the relatively high ionic conductivity of PVDF as a ferroelectric material should take the main responsibility [22]. In addition, the TiO_2/PVDF@MoS_2 fiber has lower PL intensity compared to the MoS_2/PVDF fiber, which was attributed to the core-shell heterostructure, indicating that the recombination of photo-generated electron-holes was suppressed effectively. Therefore, the TiO_2/PVDF@MoS_2 could effectively enhance the separation of photo-generated charge carriers and extend the lifetime of photo-generated electron-hole pairs, leading to the superior photocatalytic activity.
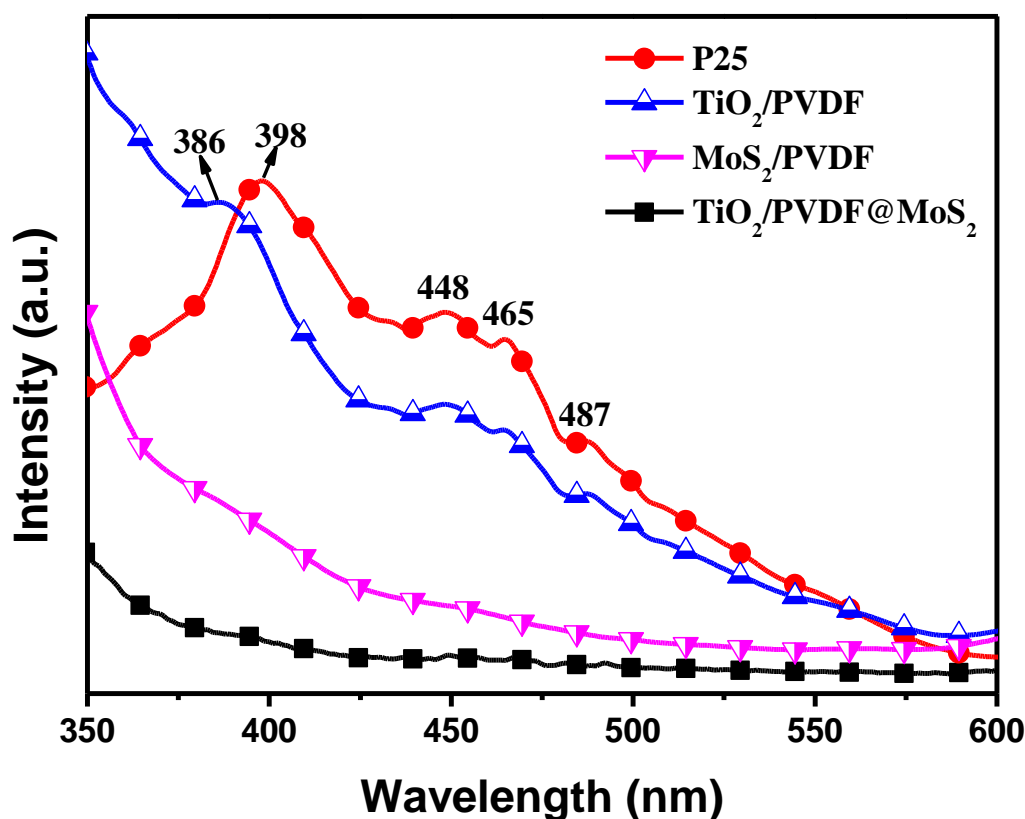
Figure 8. PL spectra of P25, TiO_2/PVDF, MoS_2/PVDF and TiO_2/PVDF@MoS_2.

3.4. Photocatalytic Performances

The photocatalytic performances of the as-prepared samples have been investigated by monitoring the time-dependent absorbance changes of RhB under visible light irradiation by using a white LED lamp. Figure 9a shows the time-dependent absorbance changes of RhB at 554 nm for RhB without photocatalyst, P25, TiO_2/PVDF, MoS_2/PVDF and TiO_2/PVDF@MoS_2, respectively. As can be seen, the absorbance of RhB without photocatalyst was almost unchanged under visible light illumination for 120 min, indicating that RhB was stable under visible light. Compared with the MoS_2/PVDF reaction system, the TiO_2/PVDF@MoS_2 reaction system exhibited a superior photocatalytic efficiency, which was attributed to the core-shell heterostructure. Surprisingly, the P25 and TiO_2/PVDF reaction systems both had good catalytic efficiency since they can only absorb UV light, as discussed in the UV-Vis section. Specifically, the TiO_2/PVDF reaction system seemed to have the highest catalytic efficiency. There were two reasons for the photocatalytic effect under visible light irradiation for P25 and TiO_2/PVDF reaction systems. On the one hand, the chromophore of RhB absorbed visible light and came to be in an excited state. Then the fast electron transferred from the excited chromophores to the conduction band of TiO_2 led to degrade the RhB [52]. On the other hand, there were some oxygen vacancies related to a defect in P25 and TiO_2/PVDF, as discussed in the PL spectra section, which could absorb visible light and lead to the degradation of RhB.
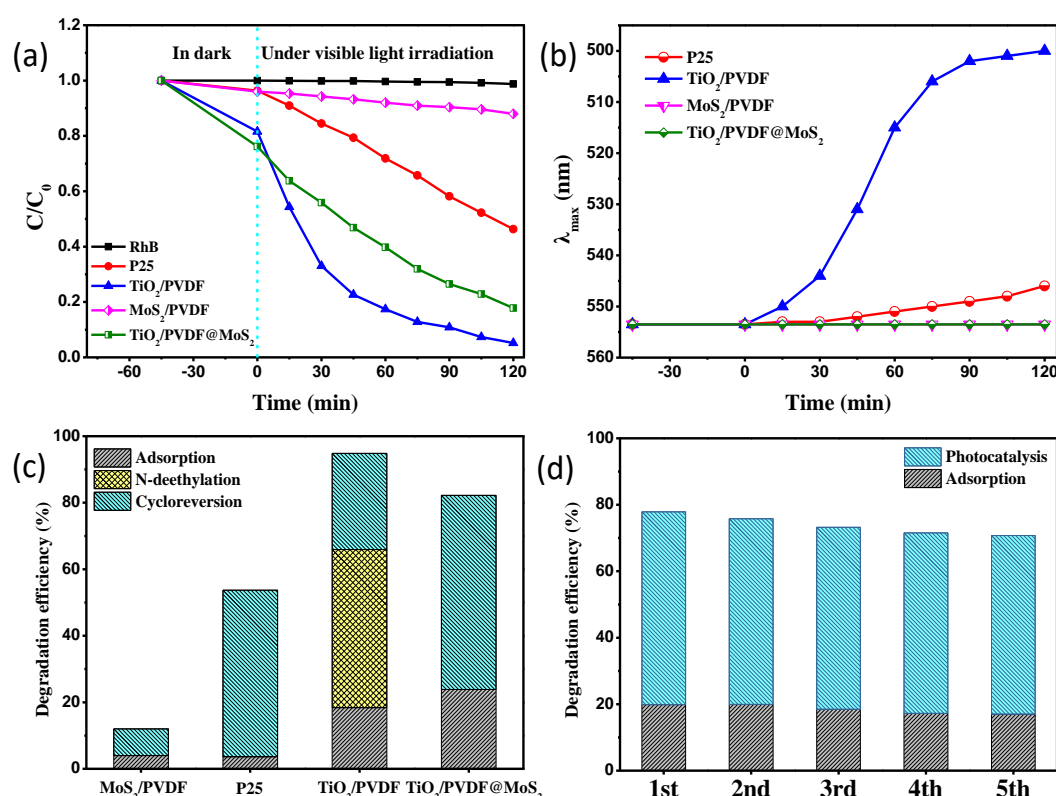
Figure 9. (**a**) Photocatalytic degradation curves of RhB over the samples: RhB without photocatalyst, P25, TiO$_2$/PVDF, MoS$_2$/PVDF and TiO$_2$/PVDF@MoS$_2$. (**b**) The wavelength of maximum absorption λ_{max} vs irradiation time. (**c**) The adsorption of RhB in dark as well as the *N*-deethylation and cycloreversion of RhB under visible light irradiation for different samples. (**d**) The degradation performance during 45-min adsorption of RhB in dark and 120-min photocatalytic degradation of RhB with the TiO$_2$/PVDF@MoS$_2$ core-shell heterostructured fibers. The experiment was repeated five times.

By carefully observing the changes of the UV-Vis spectra at different times of the resultant samples, it was easy to find that the maximum absorption peaks of RhB solution for MoS$_2$/PVDF and TiO$_2$/PVDF@ MoS$_2$ only had intensity changes rather than peak shift, as shown in Figure S5 (SI). While the maximum absorption peaks of RhB solution for P25 and TiO$_2$/PVDF had not only intensity changes, but also peak shift. By comparing the optical photographs of RhB solution at different times of TiO$_2$/PVDF and TiO$_2$/PVDF@ MoS$_2$, it could be found that the RhB solution for TiO$_2$/PVDF constantly faded and turned yellow with the increase of time, however, the corresponding RhB solution for TiO$_2$/PVDF@ MoS$_2$ just faded, as displayed in Figure S6 (SI).

The wavelength of maximum absorption λ_{max} vs irradiation time was shown in Figure 9b. It can be found that the maximum absorption λ_{max} for MoS$_2$/PVDF and TiO$_2$/PVDF@ MoS$_2$ reaction system remained unchanged, while P25 and TiO$_2$/PVDF shifted to short wavelength. There are two pathways to degrade RhB; one in the cleavage of chromospheres, and the other is the *N*-deethylation of RhB [53–55]. The products of RhB stepwise *N*-deethylation are *N,N,N'*-triethyl rhodamine (TER), *N,N'*-diethyl rhodamine (DER), *N*-ethyl rhodamine (MER) and rhodamine, respectively. The corresponding maximum absorption peaks for the products are located at 539, 522, 510, and 498 nm, respectively [56]. Therefore, part of RhB in the TiO$_2$/PVDF reaction system eventually produced rhodamine through stepwise *N*-deethylation, while the RhB in P25 reaction system was only partial *N*-deethylation and did not form any of the above four final products. It can be calculated that 47.6% of the initial RhB molecules were transformed into rhodamine with *N*-deethylation by using the absorbance and molar extinction coefficient of RhB and rhodamine at 554 and 500 nm, respectively [57,58]. Figure 9c displays the three pathways in the MoS$_2$/PVDF, P25, TiO$_2$/PVDF and

TiO_2/PVDF@MoS_2 reaction systems, adsorption, *N*-deethylation, and cycloreversion, respectively. As can be seen, TiO_2/PVDF@MoS_2 was more adsorptive than TiO_2/PVDF, owing to the larger specific surface area. Benefitting from high photogenerated electron-hole separation resulting from the core-shell heterostructure, the amount of cleavage of RhB in the TiO_2/PVDF@MoS_2 reaction system was about 58.4%, more than 8.0% of the MoS_2/PVDF reaction system, 50% of P25 reaction system, and 28.9% of TiO_2/PVDF reaction system, respectively. Although the TiO_2/PVDF reaction system showed a 76.5% degradation rate in Figure 9a, 47.6% degraded, RhB was only converted to a smaller rhodamine molecule.

In order to test the reusability of TiO_2/PVDF@MoS_2 core-shell heterostructured fibers, the recycled experiments were performed by using TiO_2/PVDF@MoS_2 core-shell heterostructured fibers five times and depicted in Figure 9d. Obviously, the TiO_2/PVDF@MoS_2 core-shell heterostructured fibers still maintained high adsorption and photocatalytic properties after repeated use five times. Besides, it can be seen that the adsorption and photocatalytic properties of the TiO_2/PVDF@MoS_2 core-shell heterostructured fibers decreased slightly with the increase of the reuse times, which was attributed to the loss of the photocatalyst on the fibers surface in the rinsing process in recovery.

The flexible characteristic was of great practical significance in recycling and reuses processes for photocatalytic materials. For the powdery photocatalysts, an inevitable problem was the loss of the photocatalyst during the separation process, leading to difficulties in recycle and reuse processes. In addition, some fibrous photocatalysts prepared by electrospinning generally required a high temperature to remove the organic components in the fibers, which resulted in very brittle fibrous photocatalysts. When these brittle fibrous photocatalysts were used in the photocatalytic experiments, the photocatalysts would be broken and lost due to being stirred, and thus couldn't be recycled and reused.

For the flexible TiO_2/PVDF@MoS_2 core-shell heterostructured fibers synthesized in this work, the presence of PVDF and a low temperature hydrothermal synthesis could keep it very flexible. Therefore, after five repeated uses, the photocatalytic performance of the flexible TiO_2/PVDF@MoS_2 core-shell heterostructured fibers was only slightly reduced due to the shedding of a few photocatalysts. In addition, the separation of the flexible TiO_2/PVDF@MoS_2 core-shell heterostructured fibers from the reaction system was very simple. It only needed to be clipped directly from the reaction system, which had a very important practical application value.

In order to further investigate the photocatalytic performance of the as-prepared samples, the photocatalytic degradation of LVFX which only absorbs UV light was carried out, as displayed in Figure 10. As can be seen, the absorbance of LVFX without photocatalyst remained unchanged under white light LED illumination for 120 min. Obviously, the as-obtained TiO_2/PVDF@MoS_2 core-shell heterostructured fibers still had the best photocatalytic properties in three kinds of photocatalysts, which was attributed to relatively large adsorption and high photogenerated electron-hole separation owing to the core-shell heterostructure. Meanwhile, MoS_2/PVDF showed a very weak photocatalytic performance, except for the relatively large adsorption capacity. Surprisingly, TiO_2/PVDF exhibited better photocatalytic performance than MoS_2/PVDF under visible light irradiation. Taking into account the band-gap of TiO_2/PVDF fibers and the spectrum of LED white light used in the experiment, the photocatalytic activity of TiO_2/PVDF fibers membrane on LVFX was mainly attributed to the absorption of visible light by defects in TiO_2/ PVDF fibers discussed earlier.
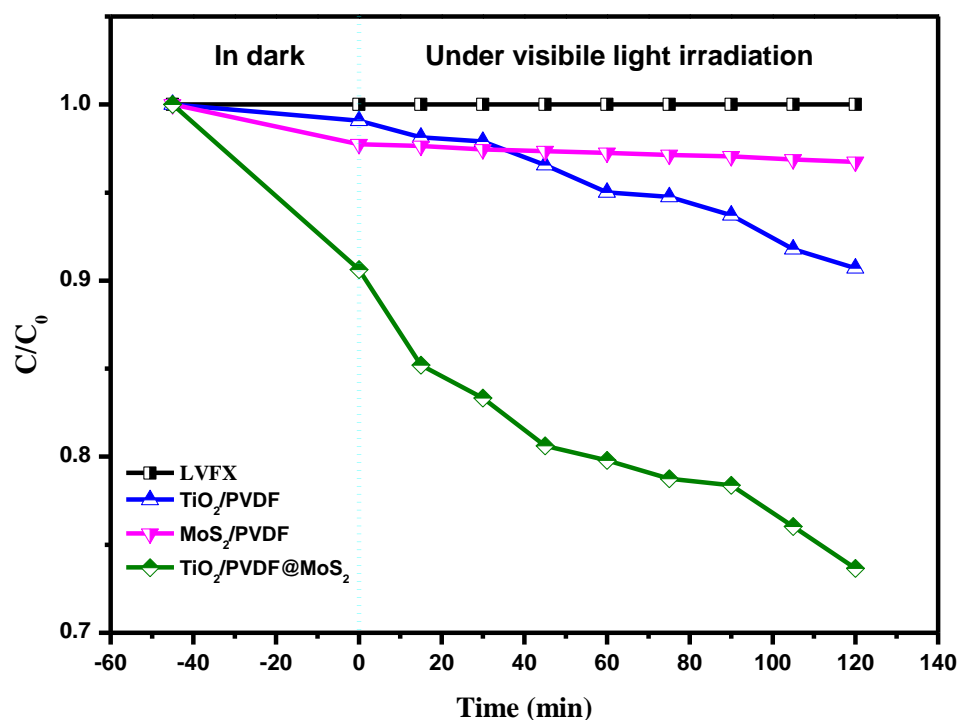
Figure 10. Photocatalytic degradation curves of LVFX over the samples: LVFX without photocatalyst, $TiO_2/PVDF$, $MoS_2/PVDF$ and $TiO_2/PVDF@MoS_2$.

3.5. Photocatalytic Mechanism

Generally, h^+, $OH^\bullet$ and $O_2^{-\bullet}$ were recognized as the primary active species in the photocatalytic reaction [59]. To investigate the photocatalytic mechanism of the $TiO_2/PVDF$ and $TiO_2/PVDF@MoS_2$ fibers, control experiments with addition of individual scavengers for h^+, $OH^\bullet$ and $O_2^{-\bullet}$ were conducted on the photodegradation of RhB.

As shown in Figure 11a, the degradation of RhB was suppressed slightly by adding the N_2 ($O_2^{-\bullet}$ scavenger) to the $TiO_2/PVDF$ reaction system, indicating the $O_2^{-\bullet}$ radical species, not main active oxidizing species in the photocatalytic process. However, it was significantly suppressed when the EDTA (h^+ scavenger) was added, and a moderate suppressed degradation of RhB was appeared by the addition of tBuOH ($OH^\bullet$ scavenger). This result indicates that the h^+ and $OH^\bullet$ were the main active oxidizing species involved in the $TiO_2/PVDF$ reaction system, with an order of $h^+ > OH^\bullet$, during the photodegradation process.

As mentioned above, the visible light photocatalytic ability of $TiO_2/PVDF$ fibers mainly came from oxygen vacancy related defects. Under visible light irradiation, electrons were excited from the valence band (VB) of TiO_2 and trapped by defects, forming holes in the VB. The photo-generated holes migrated to the surface of the $TiO_2/PVDF$ fibers. On the one hand, parts of photo-generated holes were directly involved in oxidizing organic contaminants. On the other hand, parts of photo-generated holes reacted with water molecules to form $OH^\bullet$ [26]. Therefore, the addition of EDTA not only inhibits the h^+ from participating in the oxidation of organic contaminants, but also inhibits the transformation of h^+ into $OH^\bullet$. The addition of tBuOH prefers to inhibit $OH^\bullet$ to participate in the oxidation reaction rather than inhibit the participation of h^+ in the oxidation process. Therefore, the addition of EDTA had a greater effect on the photodegradation of RhB than that of the addition of tBuOH. As described above, the photo-generated electrons in the TiO_2 were trapped by the defects, so that very few photo-generated electrons migrated to the surface to react with the oxygen molecules in the reaction system to form $O_2^{-\bullet}$. Therefore, the addition of N_2 had little effect on photodegradation of RhB.
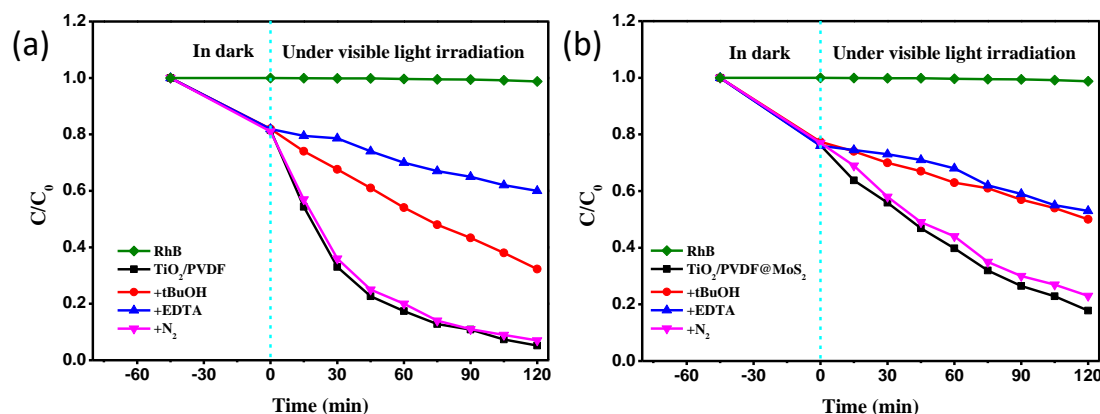
Figure 11. Control experiments with radical scavengers. (**a**) The relative concentration variation plots of RhB solution using TiO_2/PVDF fibers as the photocatalyst. (**b**) The relative concentration variation plots of RhB solution using TiO_2/PVDF@MoS_2 fibers as the photocatalyst.

The photodegradation of RhB in the TiO_2/PVDF@MoS_2 reaction system with the addition of scavenger was displayed in Figure 11b. Similar to the TiO_2/PVDF reaction system, the addition of EDTA had a stronger suppression on photodegradation of RhB than that of the addition of tBuOH and N_2 in the TiO_2/PVDF@MoS_2 reaction system. Slightly different was that the inhibition of photodegradation of RhB with the addition of tBuOH in the TiO_2/PVDF@MoS_2 reaction system was very close to that of the addition of EDTA.

To further understand this result, a schematic illustration for the photo-induced electron-hole separation and transfer process between TiO_2/PVDF core and MoS_2 shell is shown in Figure 12. Under visible light irradiation, electrons were excited from the valence band of MoS_2 to its conduction band (CB), leaving a hole in the valence band. Since the VB of TiO_2 was lower than that of MoS_2, the photo-generated electrons were transferred from the CB of MoS_2 to the CB of TiO_2. [60] Accordingly, the holes migrated from the VB of TiO_2 to the VB of MoS_2. As a consequence, the photo-generated charge carriers were separated at the core-shell interface of the TiO_2/PVDF@MoS_2 heterostructure, as illustrated in Figure 12. As the h^+ transported to the VB of MoS_2 from the VB of TiO_2, most of the h^+ oxidized the water molecules in the solution to form $OH^\bullet$ [14] due to the relatively large specific surface area of TiO_2/PVDF@MoS_2 fiber compared to TiO_2/PVDF fiber. On the other hand, a small portion of h^+ was directly involved in the oxidation of organic contaminants. Hence, a close inhibitory effect on the photodegradation of RhB appeared in the addition of tBuOH compared the addition of EDTA. Meanwhile, the photo-generated electrons were transported to the CB of TiO_2. Since TiO_2 was in the core of the composite, only a very small number of electrons reacted with oxygen molecules in solution to form $O_2^{-\bullet}$ [61] which could participate in the reaction of oxidizing organic contaminants. Therefore, the addition of N_2 had little effect on inhibiting the photodegradation of RhB.
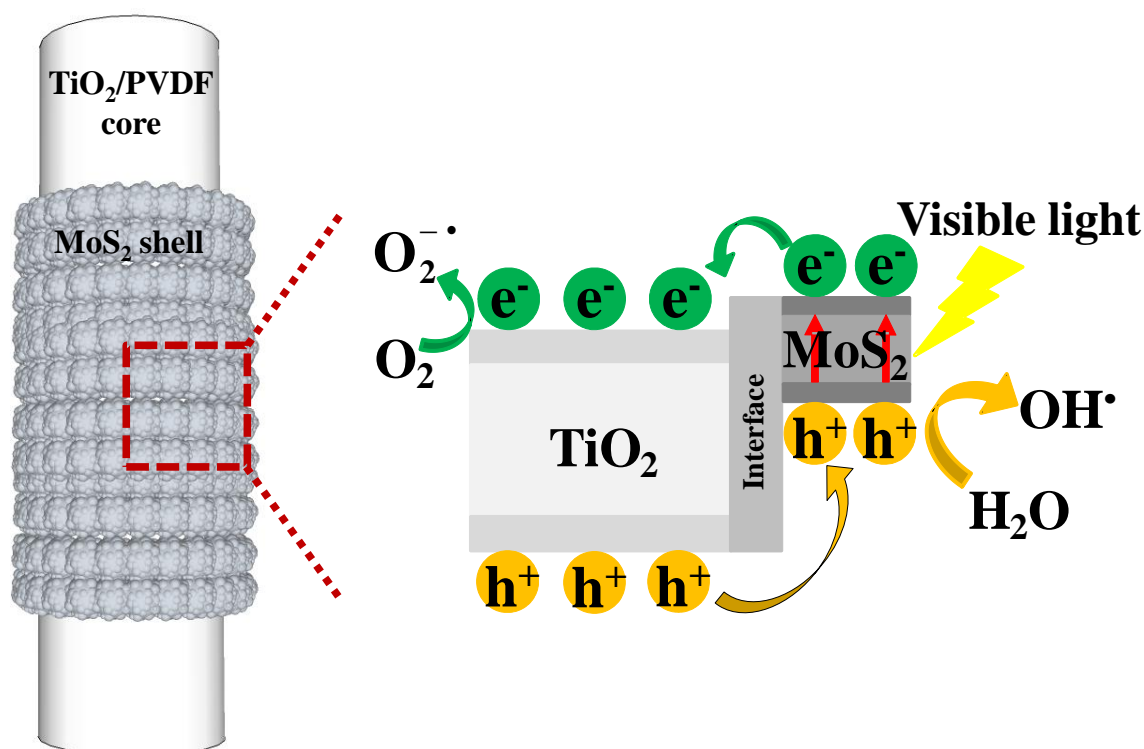
Figure 12. Schematic illustration for the photo-generated electron-hole separation and transfer process between TiO_2/PVDF core and MoS_2 shell.

3.6. Self-Cleaning Performance

The wettability of the surface determines the main cleaning mechanism. One of the main parameters to characterize the wetting behavior of the surface is the static contact angle, which is the observable angle between liquid and solid. The contact angles of H_2O, RhB, MB are 128.28°, 120.30°, 129.27°, respectively, as shown in the Figure 13a–c. Therefore, it can be obtained that the prepared TiO_2/PVDF@MoS_2 core-shell heterostructured fibers are hydrophobic to water and three dyes.

In addition, the self-cleaning properties of TiO_2/PVDF@MoS_2 core-shell heterostructured fibers were tested by dropping 10 mg·L^{-1} of RhB and MB onto the surface of the as-prepared product under visible light illumination, as depicted in Figure 13d–s. It can be easily found that the colors of these two dyes almost disappear in about 150 min, meaning a good self-cleaning performance to these two dyes.

Furthermore, due to the hydrophobicity of TiO_2/PVDF@MoS_2 core-shell heterostructured fibers surface, water droplets can remain on the surface of the sample. Therefore, the dust can be removed from the sample surface by rolling the water droplets on the sample surface to achieve self-cleaning effect. As displayed in Figure S7 (SI), before dropping water onto the surface of the sample, a layer of dust is sprayed on the sample surface. Then, the droplets are then dropped onto the surface of the sample. Slightly tilted sample, droplets roll on its surface and bring dust down to reveal the original surface of the sample. This means that in the actual use, the as-prepared products can remove the adhered dyes or dust by sunlight or rainwater themselves, so as to reduce maintenance costs.
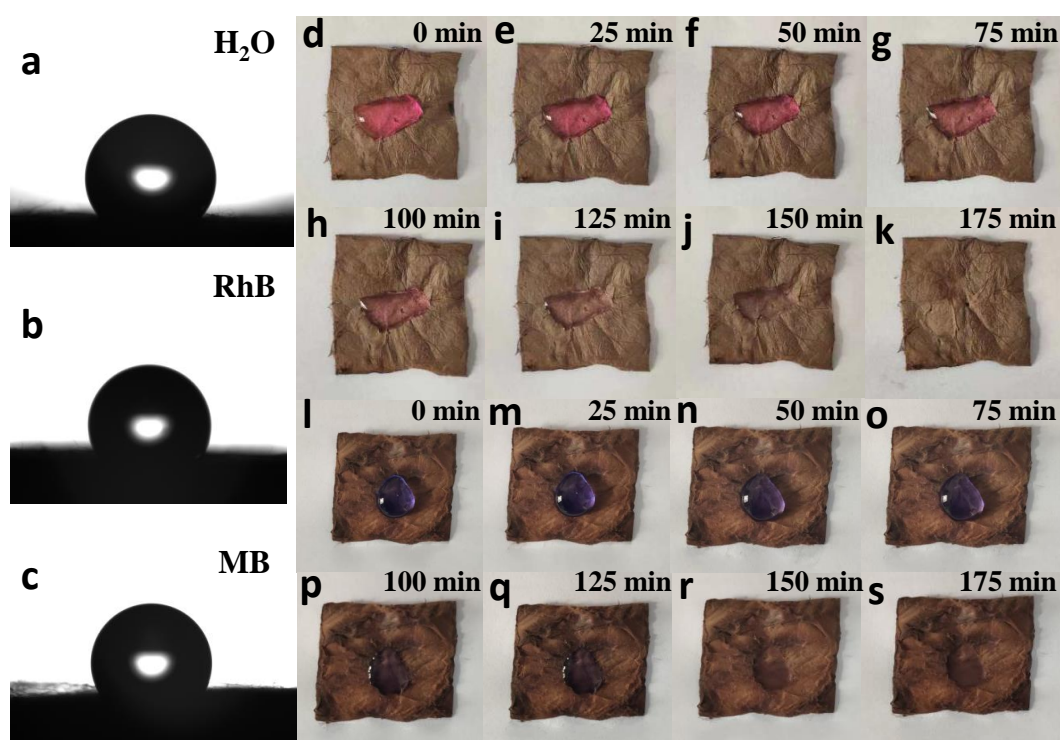
Figure 13. The optical images taken while the water and dye droplets come into contact to the surface of TiO_2/PVDF@MoS_2 core-shell heterostructured fibers (**a–c**). Photographs of the RhB (**d–k**) and MB (**l–s**) droplet on the surface of TiO_2/PVDF@MoS_2 core-shell heterostructured fibers under visible light illumination.

4. Conclusions

Novel flexible, recyclable, and reusable TiO_2/PVDF@MoS_2 fibers with core-shell heterostructures were synthesized by one-step low temperature hydrothermal method on the basis of TBOT/PVDF fibers prepared by electrospinning. The as-prepared core-shell heterostructured TiO_2/PVDF@MoS_2 fibers have good visible light absorption performance owing to the addition of narrow bandgap MoS_2. As the core-shell heterostructure can greatly improve the photo-generated electron-hole pair's separation efficiency, the as-prepared core-shell heterostructured TiO_2/PVDF@MoS_2 fibers have a very high dye contamination and antibiotic removal rates compared to the TiO_2/PVDF fibers, under white light LED irradiation. Different from the main path way that the *N*-deethylation accompanied by cycloreversion to degrade RhB with TiO_2/PVDF fibers, the path way to remove RhB with TiO_2/PVDF@MoS_2 core-shell heterostructured fibers is mainly the cleavage effect on chromospheres ring, which is a more complete degradation. Furthermore, the h^+ was recognized as the most active species in the oxidation of organic pollutants. The results show that the as-prepared product has good photocatalytic activity and self-cleaning performance under visible light. Due to the presence of the PVDF polymer inside TiO_2/PVDF@MoS_2 the fiber membrane, the TiO_2/PVDF@MoS_2 core-shell heterostructured fiber has good flexibility and reusability, making itself a prospective material in the field of environmental management.

References

1. Xiang, Q.; Yu, J.; Jaroniec, M. Synergetic Effect of MoS_2 and Graphene as Cocatalysts for Enhanced Photocatalytic H_2 Production Activity of TiO_2 Nanoparticles. *J. Am. Chem. Soc.* **2012**, *134*, 6575–6578. [CrossRef] [PubMed]

2. Ding, Q.; Meng, F.; English, C.R.; Cabán-Acevedo, M.; Shearer, M.J.; Liang, D.; Daniel, A.S.; Hamers, R.J.; Jin, S. Efficient Photoelectrochemical Hydrogen Generation Using Heterostructures of Si and Chemically Exfoliated Metallic MoS_2. *J. Am. Chem. Soc.* **2014**, *136*, 8504–8507. [CrossRef] [PubMed]

3. Wang, D.; Xu, Y.; Sun, F.; Zhang, Q.; Wang, P.; Wang, X. Enhanced photocatalytic activity of TiO_2 under sunlight by MoS_2 nanodots modification. *Appl. Surf. Sci.* **2016**, *377*, 221–227. [CrossRef]

4. Sotelo-Vazquez, C.; Quesada-Cabrera, R.; Ling, M.; Scanlon, D.O.; Kafizas, A.; Thakur, P.K.; Lee, T.; Taylor, A.; Watson, G.W.; Palgrave, R.G.; et al. Evidence and Effect of Photogenerated Charge Transfer for Enhanced Photocatalysis in WO_3/TiO_2 Heterojunction Films: A Computational and Experimental Study. *Adv. Funct. Mater.* **2017**, 1605413. [CrossRef]

5. Low, J.; Dai, B.; Tong, T.; Jiang, C.; Yu, J. In Situ Irradiated X-Ray Photoelectron Spectroscopy Investigation on a Direct Z-Scheme TiO_2/CdS Composite Film Photocatalyst. *Adv. Mater.* **2019**, *31*, 1802981. [CrossRef]

6. Li, L.; Ya, J.; Xiang, L.; Liu, Z.; Lei, E. The preparation of CuS/TiO_2 nanotube arrays with high-active under visible light by ultrasonic-assisted hydrothermal method. *Appl. Phys. A* **2017**, *123*, 667. [CrossRef]

7. Chen, G.; Song, X.; Guan, L.; Chai, J.; Zhang, H.; Wang, S.; Pan, J.; Tao, J. Defect Assisted Coupling of a MoS_2/TiO_2 Interface and Tuning of Its Electronic Structure. *Nanotechnology* **2016**, *27*, 355203. [CrossRef] [PubMed]

8. Chen, X.; Selloni, A. Introduction: Titanium Dioxide (TiO_2) Nanomaterials. *Chem. Rev.* **2014**, *114*, 9281–9282. [CrossRef]

9. Zhou, W.; Sun, F.; Pan, K.; Tian, G.; Jiang, B.; Ren, Z.; Tian, C.; Fu, H. Well-ordered Large-pore Mesoporous Anatase TiO_2 with Remarkably High Thermal Stability and Improved Crystallinity: Preparation, Characterization, and Photocatalytic Performance. *Adv. Funct. Mater.* **2011**, *21*, 1922–1930. [CrossRef]

10. Zhang, W.; Xiao, X.; Zheng, L.; Wan, C. Fabrication of TiO_2/MoS_2 Composite Photocatalyst and Its Photocatalytic Mechanism for Degradation of Methyl Orange under Visible Light. *Can. J. Chem. Eng.* **2015**, *93*, 1594–1602. [CrossRef]

11. Radisavljevic, B.; Radenovic, A.; Brivio, J.; Giacometti, V.; Kis, A. Single-layer MoS_2 Transistors. *Nat. Nanotechnol.* **2011**, *6*, 147–150. [CrossRef] [PubMed]

12. Zeng, H.; Dai, J.; Yao, W.; Xiao, D.; Cui, X. Valley Polarization in MoS_2 Monolayers by Optical Pumping. *Nat. Nanotechnol.* **2012**, *7*, 490–493. [CrossRef] [PubMed]

13. Zheng, L.; Han, S.; Liu, H.; Yu, P.; Fang, X. Hierarchical MoS_2 Nanosheet@TiO_2 Nanotube Array Composites with Enhanced Photocatalytic and Photocurrent Performances. *Small* **2016**, *12*, 1527–1536. [CrossRef] [PubMed]

14. Liu, X.; Xing, Z.; Zhang, H.; Wang, W.; Zhang, Y.; Li, Z.; Wu, X.; Yu, X.; Zhou, W. Fabrication of 3D Mesoporous Black $TiO_2/MoS_2/TiO_2$ Nanosheets for Visible-light-driven Photocatalysis. *ChemSusChem* **2016**, *9*, 1118–1124. [CrossRef] [PubMed]

15. Hofstadler, K.; Bauer, R.; Novalic, S.; Heisler, G. New Reactor Design for Photocatalytic Wastewater Treatment with TiO_2 Immobilized on Fused-Silica Glass Fibers: Photomineralization of 4-Chlorophenol. *Environ. Sci. Technol.* **1994**, *28*, 670–674. [CrossRef] [PubMed]

16. Fan, W.; Lai, Q.; Zhang, Q.; Wang, Y. Nanocomposites of TiO_2 and Reduced Graphene Oxide as Efficient Photocatalysts for Hydrogen Evolution. *J. Phys. Chem. C* **2011**, *115*, 10694–10701. [CrossRef]

17. Yu, D.; Bai, J.; Gu, Y.; Li, C. Solvothermal Synthesis of TiO_2/CNFs Heterostructures with Photocatalytic Activity. *NANO Brief Rep. Rev.* **2015**, *10*, 1550080. [CrossRef]

18. He, T.; Bahi, A.; Zhou, W.; Ko, F. Electrospun Nanofibrous Ag-TiO_2/Poly(vinylidene fluoride) (PVDF) Membranes with Enhanced Photocatalytic Activity. *J. Nanosci. Nanotechnol.* **2016**, *16*, 7388–7394. [CrossRef]

19. Zhang, X.; Shao, C.; Li, X.; Miao, F.; Wang, K.; Lu, N.; Liu, Y. 3D MoS_2 Nanosheet/TiO_2 Nanofiber Heterostructures with Enhanced Photocatalytic Activity under UV Irradiation. *J. Alloys Compd.* **2016**, *686*, 137–144. [CrossRef]

20. Sun, C.; Wang, N.; Zhou, S.; Hu, X.; Zhou, S.; Chen, P. Preparation of Self-supporting Hierarchical Nanostructured Anatase/rutile Composite TiO_2 Film. *Chem. Commun.* **2008**, *28*, 3293–3295. [CrossRef]

21. Lin, Z.; Li, J.; Zheng, Z.; Li, L.; Yu, L.; Wang, C.; Yang, G. A Floating Sheet for Efficient Photocatalytic Water Splitting. *Adv. Energy Mater.* **2016**, 1600510. [CrossRef]

22. Tan, J.Z.Y.; Zeng, J.; Kong, D.; Bian, J.; Zhang, X. Growth of Crystallized Titania from the Cores of Amorphous Tetrabutyl Titanate@PVDF Nanowires. *J. Mater. Chem.* **2012**, *22*, 18603–18608. [CrossRef]

23. Hay, A.A.; Mousa, H.M.; Khan, A.; Vanegas, P.; Lim, J.H. TiO_2 Nanorods Coated onto Nylon 6 Nanofibers using Hydrothermal Treatment with Improved Mechanical properties. *Colloids Surf. A Physicochem. Eng. Asp.* **2014**, *457*, 275–281.

24. Yu, D.; Bai, J.; Liang, H.; Wang, J.; Li, C. A New Fabrication of AgX (X=Br, I)-TiO_2 Nanoparticles Immobilized on Polyacrylonitrile (PAN) Nanofibers with High Photocatalytic Activity and Renewable Property. *RSC Adv.* **2015**, *5*, 91457–91465. [CrossRef]

25. Liu, F.; Hashim, N.A.; Liu, Y.; Abed, M.R.M.; Li, K. Progress in the Production and Modification of PVDF Membranes. *J. Membr. Sci.* **2011**, *375*, 1–27. [CrossRef]

26. Zhang, Z.; Liu, H.; Zhang, B.; Zhang, J.; Liu, R.; Ning, X.; Long, Y. Synthesis and Application of Highly Ordered Arrays of TiO_2 Rods Grown on Electrospun PVDF Fibers. *Mater. Res. Express* **2017**, *4*, 075907. [CrossRef]

27. Tang, W.; Zhu, T.; Zhou, P.; Zhao, W.; Wang, Q.; Feng, G.; Yuan, H. Poly (vinylidene fluoride)/poly (methyl methacrylate)/TiO_2 Blown Films: Preparation and Surface Study. *J. Mater. Sci.* **2011**, *46*, 6656–6663. [CrossRef]

28. Mohammadi, B.; Yousefi, A.A.; Bellah, S.M. Effect of Tensile Strain Rate and Elongation on Crystalline Structure and Piezoelectric Properties of PVDF Thin Films. *Polym. Test.* **2007**, *26*, 42–50. [CrossRef]

29. Tian, B.; Chen, F.; Zhang, J.; Anpo, M. Influences of Acids and Salts on the Crystalline Phase and Morphology of TiO_2 Prepared under Ultrasound Irradiation. *J. Colloid Interface Sci.* **2006**, *303*, 142–148. [CrossRef]

30. Zong, X.; Yan, H.; Wu, G.; Ma, G.; Wen, F.; Wang, L.; Li, C. Enhancement of Photocatalytic H_2 Evolution on CdS by Loading MoS_2 as Cocatalyst under Visible Light Irradiation. *J. Am. Chem. Soc.* **2008**, *130*, 7176–7177. [CrossRef]

31. Dong, B.; Liu, Y.; Han, G.; Hu, W.; Chai, Y.; Liu, Y.; Liu, C. Facile Synthesis of MoS_2 Modified TiO_2 Nanospheres with Enhanced Photoelectrocatalytic Activity. *Int. J. Electrochem. Sci.* **2016**, *11*, 3039–3049. [CrossRef]

32. Song, X.; Chen, G.; Guan, L.; Zhang, H.; Tao, J. Interfacial Engineering of MoS_2/TiO_2 Hybrids for Enhanced Electrocatalytic Hydrogen Evolution Reaction. *Appl. Phys. Express* **2016**, *9*, 095801. [CrossRef]

33. Zhou, W.; Yin, Z.; Du, Y.; Huang, X.; Zeng, Z.; Fan, Z.; Liu, H.; Wang, J.; Zhang, H. Synthesis of Few-layer MoS_2 Nanosheet-coated TiO_2 Nanobelt Heterostructures for Enhanced Photocatalytic Activities. *Small* **2013**, *9*, 140–147. [CrossRef]

34. Milella, E.; Cosentino, F.; Licciulli, A.; Massaro, C. Preparation and Characterisation of Titania/hydroxyapatite Composite Coatings Obtained by Sol-gel Process. *Biomaterials* **2001**, *22*, 1425–1431. [CrossRef]

35. Yu, J.; Zhao, X. Effect of Surface Treatment on the Photocatalytic Activity and Hydrophilic Property of the Sol-gel Derived TiO_2 Thin Films. *Mater. Res. Bull.* **2001**, *36*, 97–107. [CrossRef]

36. Liu, C.; Wang, L.; Tang, Y.; Luo, S.; Liu, Y.; Zhang, S.; Zeng, Y.; Xu, Y. Vertical Single or Few-layer MoS_2 Nanosheets Rooting into TiO_2 Nanofibers for Highly Efficient Photocatalytic Hydrogen Evolution. *Appl. Catal. B Environ.* **2015**, *164*, 1–9. [CrossRef]

37. Liao, S.; Huang, D.; Yu, D.; Su, Y.; Yuan, G. Preparation and Characterization of ZnO/TiO_2, SO_4^{2-}/ZnO/TiO_2 Photocatalyst and Their Photocatalysis. *J. Photochem. Photobiol. A Chem.* **2004**, *168*, 7–13. [CrossRef]

38. Xu, J.; Cao, X. Characterization and Mechanism of MoS_2/CdS Composite Photocatalyst Used for Hydrogen Production from Water Splitting under Visible Light. *Chem. Eng. J.* **2015**, *260*, 642–648. [CrossRef]

39. Liu, H.; Hu, H.; Wang, J.; Niehoff, P.; He, X.; Paillard, E.; Eder, D.; Winter, M.; Li, J. Hierarchical Ternary MoO_2/MoS_2/heteroatom-doped Carbon Hybrid Materials for High-performance Lithium-ion Storage. *ChemElectroChem* **2016**, *3*, 922–932. [CrossRef]

40. Liu, N.; Guo, Y.; Yang, X.; Lin, H.; Yang, L.; Shi, Z.; Zhong, Z.; Wang, S.; Tang, Y.; Gao, Q. Microwave-assisted Reactant-protecting Strategy toward Efficient MoS_2 Electrocatalysts in Hydrogen Evolution Reaction. *ACS Appl. Mater. Interfaces* **2015**, *7*, 23741–23749. [CrossRef] [PubMed]

41. Sekiyama, H.; Kosugi, N.; Kuroda, H.; Ohta, T. Sulfur K-edge Absorption Spectra of Na_2SO_4, Na_2SO_3, $Na_2S_2O_3$, and $Na_2S_2O_x$ (x = 5–8). *Bull. Chem. Soc. Jpn.* **1986**, *59*, 575–579. [CrossRef]

42. Liu, J.; Li, Y.; Ke, J.; Wang, Z.; Xiao, H. Synergically Improving Light Harvesting and Charge Transportation of TiO_2 Nanobelts by Deposition of MoS_2 for Enhanced Photocatalytic Removal of Cr (VI). *Catalysts* **2017**, *7*, 30. [CrossRef]

43. Sing, K.S.W.; Everett, D.H.; Haul, R.A.W.; Moscou, L.; Pierotti, R.A.; Rouquerol, J.; Siemieniewska, T. Reporting Physisorption Data for Gas/solid Systems with Special Reference to the Determination of Surface Area and Porosity. *Pure Appl. Chem.* **1985**, *57*, 603–619. [CrossRef]

44. Rouquerol, J.; Avnir, D.; Fairbridge, C.W.; Everett, D.H.; Haynes, J.H.; Pernicone, N.; Ramsay, J.D.F.; Sing, K.S.W.; Unger, K.K. Recommendations for the Characterization of Porous solids. *Pure Appl. Chem.* **1994**, *66*, 1739–1758. [CrossRef]

45. Yu, C.; Yang, K.; Shu, Q.; Yu, J.C.; Cao, F.; Li, X.; Zhou, X. Preparation, characterization and photocatalytic performance of Mo-doped ZnO photocatalysts. *Sci. China Chem.* **2012**, *55*, 1802–1810. [CrossRef]

46. Khanchandani, S.; Kumar, S.; Ganguli, A.K. Comparative Study of TiO_2/CuS Core/shell and Composite Nanostructures for Efficient Visible Light Photocatalysis. *ACS Sustain. Chem. Eng.* **2016**, *4*, 1487–1499. [CrossRef]

47. Yuan, Y.; Ye, Z.; Lu, H.; Hu, B.; Li, Y.; Chen, D.; Zhong, J.; Yu, Z.; Zou, Z. Constructing Anatase TiO_2 Nanosheets with Exposed (001) Facets/layered MoS_2 Two-dimensional Nanojunctions for Enhanced Solar Hydrogen Generation. *ACS Catal.* **2016**, *6*, 532–541. [CrossRef]

48. He, H.; Lin, J.; Fu, W.; Wang, X.; Wang, H.; Zeng, Q.; Gu, Q.; Li, Y.; Yan, C.; Tay, B.K.; et al. MoS_2/TiO_2 Edge-on Heterostructure for Efficient Photocatalytic Hydrogen Evolution. *Adv. Energy Mater.* **2016**, 1600464. [CrossRef]

49. Naldoni, A.; Allieta, M.; Santangelo, S.; Marelli, M.; Fabbri, F.; Cappelli, S.; Bianchi, C.L.; Psaro, R.; Santo, V.D. Effect of Nature and Location of Defects on Bandgap Narrowing in Black TiO_2 Nanoparticles. *J. Am. Chem. Soc.* **2012**, *134*, 7600–7603. [CrossRef]

50. Abazović, N.D.; Čomor, M.I.; Dramićanin, M.D.; Jovanović, D.J.; Ahrenkiel, S.P.; Nedeljković, J.M. Photoluminescence of Anatase and Rutile TiO_2 Particles. *J. Phys. Chem. B* **2006**, *110*, 25366–25370. [CrossRef]

51. Yang, Y.; Wen, J.; Wei, J.; Xiong, R.; Shi, J.; Pan, C. Polypyrrole-Decorated Ag-TiO_2 Nanofibers Exhibiting Enhanced Photocatalytic Activity under Visible-Light Illumination. *ACS Appl. Mater. Interfaces* **2013**, *5*, 6201–6207. [CrossRef]

52. Pan, L.; Zou, J.; Zhang, X.; Wang, L. Water-mediated Promotion of Dye Sensitization of TiO_2 under Visible Light. *J. Am. Chem. Soc.* **2011**, *133*, 10000–10002. [CrossRef]

53. Che, L.; Dong, Y.; Wu, M.; Zhao, Y.; Liu, L.; Zhou, H. Characterization of Selenite Reduction by Lysinibacillus sp. ZYM-1 and Photocatalytic Performance of Biogenic Selenium Nanospheres. *ACS Sustain. Chem. Eng.* **2017**, *5*, 2535–2543. [CrossRef]

54. Yuan, L.; Yang, M.; Xu, Y. Tuning the Surface Charge of Graphene for Selfassembly Synthesis of a $SnNb_2O_6$ Nanosheet-graphene (2D-2D) Nanocomposite with Enhanced Visible Light Photoactivity. *Nanoscale* **2014**, *6*, 6335–6345. [CrossRef]

55. Hu, X.; Mohamood, T.; Ma, W.; Chen, C.; Zhao, J. Oxidative Decomposition of Rhodamine B Dye in the Presence of VO_2^+ and/or Pt (IV) under Visible Light Irradiation: *N*-deethylation, Chromophore Cleavage, and Mineralization. *J. Phys. Chem. B* **2006**, *110*, 26012–26018. [CrossRef]

56. Zhuang, J.; Dai, W.; Tian, Q.; Li, Z.; Xie, L.; Wang, J.; Liu, P. Photocatalytic Degradation of RhB over TiO_2 Bilayer Films: Effect of Defects and Their Location. *Langmuir* **2010**, *26*, 9686–9694. [CrossRef]

57. Kim, Y.; Kim, H.; Jang, D. Facile Microwave Fabrication of CdS Nanobubbles with Highly Efficient Photocatalytic Performances. *J. Mater. Chem. A* **2014**, *2*, 5791–5799. [CrossRef]

58. Watanabe, T.; Takizawa, T.; Honda, K. Photocatalysis through Excitation of Adsorbates. 1. Highly efficient *N*-deethylation of Rhodamine B Adsorbed to Cadmium Sulfide. *J. Phys. Chem.* **1977**, *81*, 1845–1851. [CrossRef]

59. Teng, W.; Wang, Y.; Huang, H.; Li, X.; Tang, Y. Enhanced Photoelectrochemical Performance of MoS_2 Nanobelts-loaded TiO_2 Nanotube Arrays by Photo-assisted Electrodeposition. *Appl. Surf. Sci.* **2017**, *425*, 507–517. [CrossRef]

60. Wang, C.; Lin, H.; Liu, Z.; Wu, J.; Xu, Z.; Zhang, C. Controlled Formation of TiO_2/MoS_2 Core–shell Heterostructures with Enhanced Visible-light Photocatalytic Activities. *Part. Part. Syst. Charact.* **2016**, *33*, 221–227. [CrossRef]

61. Li, C.; Zhang, S.; Zhou, Y.; Li, J. A Situ Hydrothermal Synthesis of a Two-dimensional MoS_2/TiO_2 Heterostructure Composite with Exposed (001) Facets and Its Visible-light Photocatalytic Activity. *J. Mater. Sci. Mater. Electron.* **2017**, *28*, 9003–9010. [CrossRef]